Direct Raman Imaging Techniques for Studying the Subcellular Distribution of a Drug

*Jian Ling[1]
Steven D. Weitman[2]
Michael A. Miller[1]
Rodney V. Moore[2]
Alan C. Bovik[3]

[1]Southwest Research Institute, Bioengineering Department
6220 Culebra Rd., San Antonio, Texas 78238, USA

[2]Institute for Drug Development
14960 Omicron Dr., San Antonio, Texas 78245, USA

[3]The University of Texas at Austin
Department of Electrical and Computer Engineering
Austin, Texas 78712, USA

* Correspondence to:
Jian Ling, Ph.D.
Bioengineering Department
Southwest Research Institute
6220 Culebra Road
San Antonio, TX 78238
Tel: (210) 522-3953
Fax: (210) 684-6147
Email: jling@swri.org

ABSTRACT

Direct Raman imaging techniques are demonstrated to study the drug distribution in living cells. The advantage of Raman imaging is that no external markers are required, which simplify the sample preparation and minimally disturbs the drug mechanism during imaging. The major challenge in Raman imaging is the very weak Raman signal. In this study, we presented a Raman image model to describe the degradation of Raman signals by imaging processes. Using this model, special-purpose image-processing algorithms were demonstrated to restore the Raman images. The processing techniques were then applied to visualize the anticancer agent paclitaxel in living MDA-435 breast cancer cells. Raman images were obtained from a cancer cell before, during, and after the drug treatment. The paclitaxel distribution illustrated in these images is explained by the binding characteristics of the paclitaxel and its molecular target – the microtubules. This result demonstrates that direct Raman imaging is a promising tool to study the distribution of a drug in living cells.

INTRODUCTION

The recent implementation of rational drug design, combinatorial chemistry techniques, and high throughput screening have led to large numbers of new drug leads. There is a tremendous need for cost-effective and efficient approaches to evaluate the efficacy of these potential drugs. Early assessment of drug efficacy is critical for pharmaceutical companies because it will save millions of dollars that would otherwise be spent on animal and clinical studies on less efficient drug leads.

A cost-effective way of evaluating drug efficacy at the early stage of drug development is to understand its action at the cellular level [1, 2]. For example, the cellular uptake, intracellular distribution, binding characteristics, intracellular pharmacokinetics, and cellular resistance of a drug generally determine the efficacy of the drug.

Laser scanning fluorescence microscopy has been used for the *in vitro* study of drug action at the cellular level for many years [3-10]. However, the auto-fluorescence of most drugs is weak and unspecific (broad bandwidth), therefore, molecular-specific images often cannot be acquired by imaging of auto-fluorescence. Instead, certain fluorophores need to be used as a fluorescing label to selectively bind to specific regions of the drug molecules by chemical or physical means before imaging [11, 12]. The need to prepare and, subsequently, test external markers or labels often complicates the assessment of drug action. In addition, using a relatively large fluorophore molecule as a tag on to a (often smaller) drug molecule can potentially change the activities of the drug in tumor cells. The fluorescent markers used in the specimen may cause undesirable pharmacological or toxicological effects. Also, a suitable marker is often not available

for all bio-molecules. The continuous loss of fluorescence intensity during measurement due to photon bleaching, and the potential for photo-damage to the bio-specimen due to the use of ultraviolet wavelengths, are also fundamental problems of fluorescence microscopy.

The Raman spectrum of a particular substance depends on the structure (vibrational states of chemical bonds) of the molecules, and therefore it can identify a particular type of molecule by its unique combination of scattered frequencies (also referred to as Raman peaks or Raman modes). Raman imaging can provide an overview of the spatial arrangement of a particular type of molecule within a heterogeneous specimen. Raman imaging requires no external markers, dyes, or labels as required in fluorescent imaging. In addition, the near-infrared excitation used in Raman imaging of the present work has a number of advantages for biological systems, such as producing less laser-induced fluorescence and photo-thermal degradation, and allowing better perspective depth (>1 mm) into a sample [13, 14].

The major challenge in Raman applications is the inherently weak signals in Raman scattering comparing to the signals in Rayleigh scattering or fluorescence. Raman imaging, especially direct Raman imaging, was not practical until the recent development of robust laser sources and low-noise CCD (charge-coupled device) detectors [15, 16]. For many years Raman images have been acquired by pixel-to-pixel (or line-to-line) laser-scanning methods [17-22]. Because the Raman signal is weak and takes a relatively long time to obtain the spectrum for each pixel, the scanning time for a whole image is considerable. For example, complete scanning of a 128x128-pixel Raman image using

point illumination may take overnight, which is not a suitable scanning rate for living cell studies.

With the inventions of dielectric filters [23], acousto-optic tunable filters (AOTF) [24], and liquid crystal tunable filters (LCTF) [25-27], direct (or wide field) Raman imaging became an alternative imaging method. Direct Raman images are acquired at a selected Raman mode from a sample that is globally illuminated by an expanded laser beam (Figure 1). The imaging time is equivalent to the scanning time for one pixel in the laser-scanning method. In addition, the fidelity of the direct Raman images is primarily limited by the objective lens used in the microscope. Therefore, direct Raman imaging has the potential to provide an efficient way of obtaining high-definition Raman images. Direct Raman imaging has been used to study the distribution of the non-fluorescent photodynamic therapy agent cobalt-octacarboxy phthalocyanine [CoOCP] inside the K562 leukemia cells [28-30]. These studies suggest the potential application of Raman imaging in drug research. However, in order to extract correct and useful information from Raman images with weak signals, a systematic procedure is required.

In this paper, a model was first developed for direct Raman microscopic images to describe the degradation of Raman signals by several processes: non-uniform illumination of the laser excitation source, distortion by the microscope system, and the influence of additive signal-dependent Gaussian noise. Using this model, image-processing algorithms were demonstrated to restore a recorded Raman image into a considerably improved image that better reflects the molecular distributions.

The general Raman imaging and data analysis techniques were then applied to the visualization of an anticancer drug – paclitaxel within living tumor cells. Paclitaxel is an important antimitotic agent for which the mechanisms of interaction with a cell are well-established [31-34] and is a suitable candidate for validation of Raman imaging capabilities.

MODELING AND PROCESSING OF DIRECT RAMAN IMAGES

Assume a laser beam illuminates at a focal plane (z) inside a three-dimensional specimen. The Raman scattering coefficient for the heterogeneous area is *K(x,y,z)*, which is proportional to the concentration of specific chemical bonds to be imaged. The fluorescence signal from the heterogeneous specimen is $K_0(x,y,z)$. Then the scattering signal *s(x,y,z)* can be modeled as:

$$s(x,y,z) = [K(x,y,z) + K_0(x,y,z)] \times i(x,y) \times t, \quad (1)$$

where *t* is the exposure time. Usually the intensity of the illumination at the focal plane is not uniform but dependent on the locations *(x,y)* due to the imperfections in the laser expanding system. This lack of homogeneity of the illumination, indicated by *i(x,y)*, causes a non-uniform illumination effect in the recorded images.

A direct Raman image is a wide-field image that is taken at a specific focal plane within a sample. However, this image is the sum of in-focus information from the focal plane and out-of-focus information from the neighborhood planes due to the finite recording aperture and the limited depth of focus of the imaging system [35, 36]. In other words, the Raman signal *s(x,y,z)* is blurred by the microscopic system. This blur is characterized in terms of the microscope's point spread function (PSF) *h(x,y,z)* or its

Fourier transform, the optical transfer function (OTF). If the image formation system is assumed to be linear and time-invariant, then the recorded image *g(x,y,z)* can be represented as:

$$g(x,y,z) = \{h(x,y,z) * [K(x,y,z) + K_0(x,y,z)]\} \times i(x,y) \times t + n(x,y,z), \quad (2)$$

where * is the linear convolution operator. The blurred Raman signal was further degraded by the additive noise *n(x,y,z)* that occurs during image recording.

The purpose of the Raman image processing is to determine the Raman scattering coefficient *K(x,y,z)* of the imaging area from the recorded image *g(x,y,z)*. In order to determine *K(x,y,z)*, it is necessary to reduce the noise *n(x,y,z)* from the image *g(x,y,z)*, to correct the non-uniform illumination *i(x,y)*, to deconvolve with the point-spread function *h(x,y,z)*, and to subtract the fluorescence signal $K_0(x,y,z)$.

Noise Reduction Using Anisotropic Median-Diffusion Filter

A Raman image is a molecular image, which displays the distribution of molecules. Such an image can be modeled as a piecewise-smooth image, which can be divided into several regions. Each region is chosen such that the changes in molecular concentration within the region are small and gradual. The intensities between the different regions are quite dissimilar because of the significant difference in molecular concentration. For these kind of piecewise-smooth images, the anisotropic median-diffusion filter was found [37] to be a suitable denoising filter. The anisotropic median-diffusion filter is described as:

$$\begin{aligned} g^{(n+1)} &= g^{(n)} + \lambda/4 \left[c_N \nabla_N g + c_S \nabla_S g + c_E \nabla_E g + c_W \nabla_W g \right]^{(n)}, \\ g^{(n+1)} &= MedianFilter(g^{(n+1)}, Window), \end{aligned} \quad (3)$$

where *(n)* and *(n+1)* are the number of iterations, and $\lambda \in [0,1]$ controls the rate of the diffusion. The idea behind the anisotropic median-diffusion filter is to evolve from the recorded noisy image $g^{(0)}$ a family of increasingly smooth images $g^{(n)}$ to estimate the original image.

The letters *N,S,E,W* in Eq. 3 are mnemonics for North, South, East and West; they describe the direction of the local gradient. The local gradient of an image at any iteration is calculated by the difference in the nearest-neighbor pixels:

$$\begin{aligned} \nabla_N g_{i,j} &= g_{i-1,j} - g_{i,j} \\ \nabla_S g_{i,j} &= g_{i+1,j} - g_{i,j} \\ \nabla_E g_{i,j} &= g_{i,j+1} - g_{i,j} \\ \nabla_W g_{i,j} &= g_{i,j-1} - g_{i,j} \end{aligned} . \qquad (4)$$

The diffusion coefficients c_N , c_S , c_E , c_W are the function of the local gradients $\nabla_N g$, $\nabla_S g$, $\nabla_E g$, and $\nabla_W g$, respectively. The Tukey biweight norm proposed by Black *et al.* [38] is used as the diffusion function. The normalized (magnitude) Tukey biweight diffusion coefficient is defined as:

$$c(\nabla g, K) = \begin{cases} \frac{25}{16K}\left[1-\left(\nabla g/\sqrt{5}K\right)^2\right]^2 & |\nabla g| \le \sqrt{5}K \\ 0 & otherwise \end{cases}, \qquad (5)$$

where *K* is the threshold of the local gradients, which is tuned for a particular application. The *Window* in Eq. 3 is the window for the median operator. A 3x3 window is usually used.

The anisotropic median-diffusion filter is especially useful to smooth images with low signal-to-noise ratio, such as the Raman images. It can effectively reduce the Gaussian noise without blurring the edges on the images. A quantitative study has shown

that the anisotropic median-diffusion smoothed images are very close to the original images in correlation, mean luminance and contrast [37].

Correction of Non-uniform Illumination

After reducing the noise, the non-uniform illumination *i(x,y)* needs to be corrected (see Equation 2). A flat field image is used as a reference image to correct the lateral non-uniform illumination. The effect of illumination difference in the axial direction is considered in PSF.

According to the image model, a recorded flat-field reference image (after smoothing) can be expressed as:

$$r(x,y) = [h(x,y) * K_{flat}] \times i(x,y) \times t\,, \tag{6}$$

where K_{flat} is a constant here. The residue noise after smoothing is ignored in Eq. 6 for simplicity. The OTF of a microscope system is usually a low-pass filter (for example, the microscope system used in this research has a lateral cut-off frequency of 0.57 μm^{-1} and an axial cut-off frequency of 0.15 μm^{-1}). Therefore, Eq. 6 can be simplified to:

$$r(x,y) = K_{flat} \times i(x,y) \times t\,, \tag{7}$$

because of the "zero" frequency characteristics of the K_{flat}. The reference image is then normalized by its own median value to give the compensating image *c(x,y)*:

$$c(x,y) = \frac{r(x,y)}{Median[r(x,y)]} = \frac{i(x,y)}{Median[i(x,y)]}\,. \tag{8}$$

Dividing *c(x,y)* by the denoised Raman image $g_s(x,y,z)$ we get the compensated image:

$$g_c(x,y,z) = \frac{g_s(x,y,z)}{c(x,y)} = \{h(x,y,z) * [K(x,y,z) + K_0(x,y,z)]\} \times Median[i(x,y)] \times t\,. \tag{9}$$

The above compensation algorithm keeps the median intensity of the image unchanged. This algorithm is based on the assumptions that the Raman scattering coefficient is linearly related to the exposure time. It is also important to smooth the image before the compensation. Otherwise, the noise may be amplified after the compensation algorithm.

Three-dimensional Image Deconvolution

The objective of three-dimensional deconvolution is to restore the blurred image by using the PSF of the imaging system. After the deconvolution, it will reduce the in-focus-plane blurs caused by the limited aperture of the system as well as the out-of-focus-plane blurs resulted from the limited depth-of-field of the system.

Many three-dimensional deconvolution algorithms have been developed, including the inverse filter, the Wiener filter, the Nearest-Neighbor deconvolution, the constrained iterative method, and the expectation-maximization maximum-likelihood (EM-ML) deconvolution. When restoring an image with all the information at the neighborhood planes available and no noise present, the deconvolution results from all these algorithms are very similar. However, in practice, some amount of noise always exists in a recorded image, even after smoothing by the anisotropic median-diffusion filter. In addition, there are often only a few images that can be recorded at different defocus planes within a limited period of time. Especially in the case of Raman imaging of living cells, we were only able to get one image (at a specific focal plane) to represent the drug distributions using the current instrumentation. This is again due to the relatively long exposure time required for Raman imaging.

Under this no-neighborhood condition, the three-dimensional deconvolution can be performed after replicating the recorded image as the neighborhood images. This simplification is based on the assumption that there is no abrupt change among the neighborhood images. However, if the assumption is not true, the three-dimensional deconvolution will not effectively remove the blurred information from the neighborhood planes.

Different deconvolution algorithms were compared on a three-dimensional cell model under the no-neighborhood condition [39]. The EM-ML deconvolution was found to achieve better results when compared with the other algorithms. The EM-ML deconvolution was derived from the Bayesian theory with Poisson noise model. An iterative algorithm of the deconvolution, developed by Richardson and Lucy [40, 41], is described as follows:

$$f^{(n+1)}(x,y,z) = \left[\frac{g_c(x,y,z)}{h(x,y,z) * f^{(n)}(x,y,z)} * h(x,y,z) \right] f^{(n)}(x,y,z), \quad \text{and,} \quad f^{(n+1)}(x,y,z) \geq 0, \tag{10}$$

where $g_c(x,y,z)$ is a stack of two-dimensional images recorded in the experiment, $f^{(n)}(x,y,z)$ is the restored images at nth iteration, and $h(x,y,z)$ is the PSF of the imaging system. The non-negative constraint is applied to the restored images after each iteration.

Under the no-neighborhood condition in this study, the $g_c(x,y,z)$ is composed of a image recorded at the focal plane plus the neighborhood images created by replicating the focal plane image. All these images go through the denoising and non-uniform illumination correction procedures as described above.

It is also important to subtract the background, or the "DC" value from the images prior to performing the deconvolution. Studies [42, 43] have shown that the background intensity has critical influence on the performance of the EM-ML deconvolution. This is because the existence of the background makes the nonnegative constraint less effective. In this study, the image background could be the fluorescence from the aqueous solution, which can be assumed uniform across the image. This background was subtracted from $g_c(x,y,z)$ before deconvolution.

Elimination of Fluorescence Signal

After deconvolution, Equation 2 became:

$$f(x,y,z) = K(x,y,z) + K_0(x,y,z). \tag{11}$$

The next processing step is to subtract the fluorescent signal $K_0(x,y,z)$. The fluorescence signal is different from the fluorescence background discussed above. It is generated by the specimen, so it is usually non-uniform due to the heterogeneity of the specimen. The estimation of this fluorescent signal is done according to the properties of a Raman spectrum. A Raman spectrum is composed of narrow-band Raman signals and a broadband fluorescence baseline (Figure 2). The Raman signals ride on the broadband fluorescence baseline. If a Raman image is taken at the frequency of f_1, its fluorescent signal can be best estimated from another image taken at a neighborhood frequency f_2. This is because an image at neighborhood frequency f_2 shares the same fluorescence distributions as at the f_1 but without Raman signal. This neighborhood image can go through the same processing as discussed above to get the fluorescent signal $K_0(x,y,z)$, which can then be directly subtracted from Equation 11.

EXPERIMENT AND DATA ANALYSIS

Instrumentation

A Renishaw Model 2000 Raman spectroscopic system (Gloucestershire, UK, 1993) was used in the study. This system is capable of acquiring Raman spectra, laser-scanning Raman spectroscopic images, and direct Raman images with an expanded laser beam. A Ti:Sapphire laser system (Lexel Laser Inc., California) was established for the Raman system to replace the 30 mW diode laser originally equipped with the Raman system. The diode laser source is suitable for Raman spectroscopy on biological samples. However, when the laser is used for direct imaging, the beam must be expanded and spread over thousands of pixels. In such applications, it provides inadequate illumination power. In addition, the diode laser source has a line-shape beam so that the imaging area suffers severe non-uniform illumination. The Ti:Sapphire laser, pumped by a 7W argon-ion laser (Lexel 95-7), emits near-infrared wavelength with the maximum power of 1 W. The Ti:Sapphire laser also has a Gaussian beam shape which greatly improves the beam quality after beam expansion. In this study the laser was tuned to 782 nm to match the holographic notch filter in the Raman system.

The Raman system can achieve spectral resolution of 1 cm^{-1} for spectrum measurement with a grating system. For direct imaging, the dielectric filter has a bandwidth of 10-20 cm^{-1}. The Raman system is placed in a dark room and is stabilized on an anti-vibration table (Vibraplane Air Suspension System, Kinetic System, Inc., Boston, USA). This setup provides an ideal imaging environment.

A 60X Olympus water-immersion, high infrared transmission (71%) objective lens (1-UM571 LUMPLFL 60x W/IR, Olympus, Japan) was used to obtain images of living cells incubated in aqueous solution. This lens has a numerical aperture (NA) of 0.90 and a depth of field (DOF) of 1.2 μm. The diffraction-limited optical resolution of this lens can be calculated by Abbe's equation:

$$s = \frac{0.61\lambda}{NA}. \quad (12)$$

In this study, the excitation wavelength is λ = 782, the maximum resolution that can be achieved is about 0.53 μm. The resolution of the system is also affected by the magnification of the microscope, the pixel size of the CCD camera, and the sampling rate. The complete optical characteristics of the Raman system is determined by its PSF (or OTF), which was estimated in this study by using small polystyrene microspheres (0.2 μm in diameter) as the point light source[39]. This PSF will be used in three-dimensional deconvolution.

The Raman Band for Imaging the Drug

Paclitaxel is an anticancer drug often used to treat breast cancer, ovarian cancer, and non-small cell lung cancer. Paclitaxel was selected for this study because its interactions with cellular molecules have been well studied. This knowledge will help us examine the results and determine the capability of the Raman imaging technology.

Figure 3 illustrates the chemical structure of paclitaxel and its Raman spectrum of pure powder (Yunnan Hande Technology Development Co. Ltd., Kunming, China). The most significant Raman peaks of paclitaxel are at 617 cm^{-1}, 1002 cm^{-1}, and 1601 cm^{-1}.

The Raman peak at 617 cm^{-1} is due to deformation of benzene rings in the structure. The Raman peak at 1002 cm^{-1} is due to the sp^3 hybridized carbon-carbon (C-C) vibration. The Raman peak at 1601 cm^{-1} is due to the carbon-carbon double bond (C=C) stretching vibration.

The powder paclitaxel, however, is not soluble in water, thus it cannot be used to treat cells directly. According to the clinical formula of the drug (Bristol-Myers Squibb Company, Princeton, NJ), paclitaxel was first dissolved in dehydrate ethanol alcohol and cremophor EL (polyoxyethylated castor oil) and then further diluted with phosphate buffered saline (PBS) solution. With the mix of ethanol and cremophor oil, the Raman spectrum of the paclitaxel solution was affected significantly. Figure 4 illustrates the Raman spectrum (with no fluorescence baseline correction) of a 0.3mg/ml (350 μM) paclitaxel solution between 750 and 1250 cm^{-1}. The strong fluorescence baseline from cremophor oil and ethanol swamped most of the Raman peaks of paclitaxel, but leaving the peak at 1002 cm^{-1} (shift to 1000 cm^{-1}). Fortunately, neither ethanol nor cremophor oil has Raman peak around 1000 cm^{-1}.

In order to detect paclitaxel in a cell, Raman and fluorescent signals from a cell also need to be studied. In this study, the human breast tumor cell line, MDA-435, was used. Figure 5 shows the Raman spectrum (with no fluorescence baseline correction) of the cytoplasm (at one local spot) of an MDA-435 breast tumor cell. The Raman spectrum of the cell nucleus (not shown here) is very similar to the spectrum of the cytoplasm. The carbon-carbon stretching mode (at the Raman peak about 1003 cm^{-1}) from the molecules (proteins) inside cell is also presented on the cell spectrum. This peak is very close to the

1000 cm^{-1} Raman band that we will use for detecting the paclitaxel. Fortunately, the Raman signal at this peak from the cell is relatively weaker than that from the paclitaxel, thus the intrinsic Raman signal from the cell should have a small contribution to the Raman image at 1000 cm^{-1}. To further distinguish the changes of Raman signals before and after drug treatment, the Raman images before the cell exposure to the paclitaxel solution will be used as the control case to be compared with the Raman images after the drug treatment. In summary, one Raman image will be taken at 1000 cm^{-1} to detect the paclitaxel. Another Raman image will be taken at 1080 cm^{-1} to correct the contribution of fluorescent signal on the 1000 cm^{-1} image.

Cell Preparation and Imaging Procedure

Approximately 10^5 MDA-435 breast tumor cells were cultured on a gold-coated Petri dish and allowed to stabilize for 24 hours in RPMI-1640 medium supplemented with fetal bovine serum. After stabilization, the cells adhered to the bottom of the Petri dish.

Before imaging, the RPMI nutrition medium was washed out with PBS. PBS was used as the medium during imaging to reduce the fluorescent background from the nutrition medium. Three cell images were taken before paclitaxel treatment. A white light image of the cell illustrates the cell structure. A corresponding Raman image of the same cell was taken at the 1000 cm^{-1} Raman band. This image records both the Raman signal and the fluorescent signal from the cell. A second Raman image was taken at 1080 cm^{-1}, which only has the contribution from fluorescent signals. These three images form an image record under control situation.

After taking images in a control situation, PBS was then replaced by the 0.3 mg/ml (or 350 μM) paclitaxel solution to start the drug treatment. The cells were exposed to paclitaxel for one hour. During the one-hour drug treatment, the same images were recorded to show the cellular distributions of paclitaxel during the drug treatment. After one hour of treatment, the paclitaxel solution was washed out using PBS, and the cells were returned to the PBS medium. Images were then acquired to show the drug retained by the cell.

Data Processing and Analysis

As described above, each image record contains a white light image and two Raman images at 1000 cm^{-1} and 1080 cm^{-1}, respectively. An example of such a record plus the direct difference of two Raman images are shown in Figure 6. It is obviously difficult to get useful information from the raw data before processing. The image processing algorithms developed based on the Raman imaging model were then used to explore the data step by step.

Figures 7(a) and (b) illustrate the Raman images after reducing the noise using the anisotropic median-diffusion filter. The standard deviation of the image gradient was used as the threshold in diffusion coefficient. A 3x3 window was used for the median filter.

Figures 7(c) and (d) show the Raman images with the non-uniform illumination corrected. A Raman image of a flat surface was recorded before each experiment as the reference illumination.

Figures 7(e) and (f) show the images after subtracting their fluorescence background. This background is the fluorescent intensity contributed from the PBS solution. Therefore, it is uniform across the image, like a "DC" component. The fluorescent signal contributed from the intracellular structure, however, is not uniform due to the heterogeneity of the cell. That part of the fluorescence is referred to as the "AC" component in this paper. That fluorescence signal is handled in Figure 7(h).

A simple way of eliminating the fluorescence "DC" background is to subtract the average value of the image and then to set all the negative values to zero. This simplified method is only suitable when the background occupies most of the area of an image. In this case, the average value of the image is close to the "DC" background. The subtraction of average value also enhanced the image; only intensity (fluorescence "AC" component plus Raman signal) higher than the average value was left on the image. The Raman image in Figure 7(e) contains the Raman signal at the 1000 cm^{-1} band as well as the fluorescent "AC" component in this band. The image in Figure 7(f), however, contains the same fluorescent "AC" component as in the 1000 cm^{-1} band but without the Raman signal. Most importantly, the background subtraction makes the three-dimensional restoration more effective as discussed in the deconvolution section above.

Figures 7(g) and 7(h) illustrate the restored images using the EM-ML three-dimensional deconvolution algorithm. The OTF of the Raman system, determined through measurement, was used here for the deconvolution.

Finally, the Raman image at 1080 cm^{-1} in Figure 7(h) was subtracted from the Raman image at 1000 cm^{-1} in Figure 7(g). The image after eliminating the fluorescence

signal is shown in Figure 7(i), which illustrates the paclitaxel distributions. The superimposition of the paclitaxel distribution image and the white light image in Figure 6(a) is shown in Figure 7(j), which illustrates the paclitaxel distribution in the cell.

RESULTS AND DISCUSSIONS

MD-435 tumor cells were exposed to the 0.3 mg/ml (or 350 μM) paclitaxel solution for one hour. The white light images and Raman images were obtained before, during, and after the Paclitaxel treatment (Figure 8). All the Raman images were taken using a 60x water immersion lens with the exposure time of 300 seconds. They were processed using the method described above.

The first row in Figure 8 illustrates the images before drug treatment. These images show the 1000 cm^{-1} Raman signals contributed from the molecules of the cell itself. From the overlay image, the intrinsic Raman signals appear outside of the cell. It cannot be the line up problem because the white light image and Raman image are registered with 1 μm microspheres before the experiment. Most probably, the problem is due to the imaging focal plane not being at the largest cross-area of the cell. Please note there is a halo outside the cell, that may be the real cell boundary. The strong Raman signal in the corresponding Raman image could be the contribution from the neighborhood planes. This neighborhood information may not be removed effectively by the three-dimensional deconvolution due to the no-neighborhood condition (see the section of three-dimensional image deconvolution). Nevertheless, this image does show that the original Raman intensities inside this cell are relatively low.

The second and third rows in Figure 8 illustrate the images 10 minutes and 45 minutes into the drug treatment. These images suggest that the paclitaxel were accumulated outside the cell membrane and were gradually diffusing into the cell. The relative low Raman intensities in these two figures are probably because the cell is not in the PBS solution but in the drug solution, which contributes to a higher background than the PBS solution. After subtracting a higher average value from the image, its intensity became lower. In other words, the Raman intensities shown in the figures are relative after subtracting their average value. Therefore, the quantitative information was not preserved.

The fourth row through the seventh row in Figure 8 illustrate the images 10 minutes, 1.75 hours, 4 hours, and 4.5 hours after the drug treatment (after the paclitaxel agent was washed out). These images show that the Raman intensities are relatively higher in the center area as well as near the cell membrane. However, there is no intensity in the cell nucleus area. As we know, the Raman signal is directly related to the molecular concentration. The higher the intensity, the higher the molecular concentration. Therefore, these figures suggest that paclitaxel is more concentrated near the center of the cell as well as near the cell membrane, but less concentrated in the cell nucleus. The finding of paclitaxel distributions from the Raman images is explained by the binding characteristics of the paclitaxel and its molecular target – the microtubules.

Paclitaxel is an antimitotic drug, which stabilizes the microtubules, one type of cytoskeleton that plays an important role in cell division. Microtubules are long and hollow tubes of protein that grow out from a small structure near the center of the cell,

called centrosome, and extend out towards the cell periphery (Figure 9(a)). Microtubules can rapidly disassemble in one location and reassemble in another. When a cell enters mitosis (division), the microtubules disassemble and then reassemble into an intricate structure called the mitotic spindle (Figure 9(b)). The mitotic spindle provides the machinery that will segregate the chromosomes equally into the two daughter cells just before a cell divides [44]. The action of paclitaxel is to bind tightly to the growth end of the microtubules (Figure 9(c)). In this way, paclitaxel prevents the microtubules from losing subunits (i.e., depolymerization). Since new subunits can still be added (i.e., polymerization), the microtubules can grow but cannot shrink. In order for the spindle to work, the microtubules must be able not only to assemble but also to disassemble. Thus, paclitaxel prevents the mitotic spindle from functioning normally and the dividing cell is arrested in mitosis [44].

The binding mechanism of paclitaxel suggests that the high paclitaxel concentration in the center area of the cell might be the location of the centrosome (further study is needed to prove this). The relatively high paclitaxel concentration near the cell membranes is probably because the growth ends of the microtubules extend to the membrane. These patterns of paclitaxel distribution were also observed in the studies of fluorescence imaging [4, 45].

In Figure 8, it was also found that the cell started blebbing around four hours after exposure to the paclitaxel solution, and the blebs progressively increased in size. Previous studies [46-52] have shown that cell blebbing often indicates the start of cell

apoptosis (programmed death of the cell). The promotion of the assembly of microtubules after binding with paclitaxel might cause the cell blebbing.

Although the concentration of the paclitaxel solution used in this study was much higher (ten to thirty-fold) than the regular clinical concentration, it may not indicate that we cannot visualize the drug at lower concentrations. In our study, the cells were exposed to the paclitaxel solution only for a short period. The drug was washed out after one hour. In the clinical situation, however, the cells are exposed to a lower concentration of drug for a longer time. The intensity of Raman image is related to the local molecular concentrations. If, after a period of time, the drug can be accumulated locally (at the microtubules' growth end), they can still be imaged even if the treatment drug concentration is low. Experiments will continue to perform on a low drug concentration to mimic the clinical situation.

In this study, the cells were found to be not tolerable to laser power more than 15 mW, even with a short imaging time. This may due to the slow heat dissipation around the cell (this experiment was performed in room temperature). If a temperature control incubator can be used during imaging to accelerate the heat dissipation, larger excitation power may be used to increase the Raman signal. Such a temperature incubator can also provide a constant temperature environment and gas environment for the living cells.

In this study, the white light images of the cells were taken by the video camera on the Raman system, which has relatively low resolutions. The CCD camera was not used to take the white light images due to the slow switch time between the white light imaging mode and Raman imaging mode of the system. In addition, re-calibration of the

Raman tunable filter is often needed after switching back from the white light imaging mode. This re-calibration procedure is difficult to perform while monitoring the change of the drug distribution in a living cell. The future instrumentation should provide a different optical path to the CCD detector for the white light imaging. The improvement of the resolutions in white light cell images will make the drug location clearer.

CONCLUSIONS AND FUTURE DIRECTIONS

In this study, we presented and applied the direct Raman imaging techniques to visualize the drug distributions in living cells. As Raman signals are inherent to the drug molecules to be imaged, no external dyes, markers or labels are required as in radio-isotope and fluorescent imaging. This makes the sample preparation much simpler for the experiment. At the same time, the mechanism of the drug action is minimally disturbed during the experiments.

To overcome the weak signal in Raman imaging, we improved the Raman instrument by incorporating a Ti:Sapphire near-infrared laser. We presented a model to describe the degradations of Raman signals during imaging. Using this model, special-purpose image-processing algorithms were demonstrated to: 1) smooth the image noise; 2) correct the non-uniform illumination from the laser excitation source; 3) restore the blurring by the microscope system; and 4) eliminate the influence of fluorescence signals.

The general Raman imaging and data analysis techniques were then applied to the visualization of the anticancer drug paclitaxel in living tumor cells. The results show how the paclitaxel distribution changes with time in a living tumor cell. It suggested that

paclitaxel does not enter the cell nucleus, but is more concentrated around the cell centrosome and near the cell membrane. This finding is explained by the binding characteristics of the paclitaxel and its molecular target – the microtubules. Although the results presented here need to be further confirmed by other techniques, for example, using simultaneous Raman and fluorescence imaging, this study demonstrated that direct Raman imaging is a promising tool to use for determining the intracellular distribution of a drug. Based on the drug distribution, Raman imaging can be further used to study the drug mechanism, cellular uptake, resistance, and intracellular pharmacokinetics. We believe that the direct Raman imaging will become a cost-effective tool for evaluating potential drugs at the cellular level.

In this study, only qualitative Raman information was preserved in the result images. The next step is to develop methods to quantify cellular drug uptake and retention under different drug concentrations. Quantification of the intercellular drug levels would be quite valuable for evaluating the intracellular pharmacokinetics of a drug. Since the Raman signal intensity is linearly related to the concentration of the imaging molecules, we should be able to establish the relationship between intensity and concentration through a calibration procedure or by an internal standard.

We will continue to develop techniques to enhance the Raman signal. For example, the surface enhancement Raman (SERS) technique [53-56] can be applied to direct imaging. It has shown that the Raman signals can be enhanced by factors of up to 10^6 when a molecule is adsorbed on or near a nanometer-size metal particle. We believe that

the current development of nanotechnology will make the SERS technique widely available.

We will also develop a Raman imaging system so that it can simultaneously take images at several different Raman bands. The Raman signal from a single band is not unique to a molecule. It is the combination of the signals from several specific bands plus the relation of their relative intensities that is unique to a molecule. The use of one Raman band signal at 1000 cm^{-1} to detect Paclitaxel, for example, is based on the fact that the Raman signals from the cells are relatively weak. If we can acquire multiple images at several different bands, then the distribution of the molecules will be specifically determined.

ACKNOWLEDGEMENTS

This study was funded by Southwest Research Institute, San Antonio, Texas, and supported by the Institute for Drug Development at the Cancer Therapy & Research Center in San Antonio.

REFERENCES

1. E.H. Kerns, S.E. Hill, D.J. Detlefsen, K.J. Volk, B.H. Long, J. Carboni, and M.S. Lee, "Cellular uptake profile of paclitaxel using liquid chromatography tandem mass spectrometry," Rapid Communications in Mass Spectrometry. **12**, 620-624 (1998).

2. M. Dellinger, M. Geze, R. Santus, E. Kohen, C. Kohen, J.G. Hirschberg, and M. Monti, "Imaging of cells by autofluorescence: a new tool in the probing of biopharmaceutical effects at the intracellular level," Biotech. & Appl. Biochem. **28**, 25-32 (1998).

3. S.D. Baker, R.M. Wadkins, C.F. Stewart, W.T. Beck, and M.K. Danks, "Cell cycle analysis of amount and distribution of nuclear DNA topoisomerase I as determined by fluorescence digital imaging microscopy," Cytometry. **19**, 134-145 (1995).

4. C.S. Rao, J.J. Chu, R.S. Liu, and Y.K. Lai, "Synthesis and evaluation of [14C]-labelled and fluorescent-tagged paclitaxel derivatives as new biological probes," Bioorg. & Medic. Chem. **6**, 2193-2204 (1998).

5. H. Oyama, M. Nagane, S. Shibui, K. Nomura, and K. Mukai, "Intracellular distribution of CPT-11 in CPT-11-resistant cells with confocal laser scanning microscopy," Japanese J. Clini. Oncol. **22**, 331-334 (1992).

6. J.H. de Lange, N.W. Schipper, G.J. Schuurhuis, T.K. ten Kate, T.H. van Heijningen, H.M. Pinedo, J. Lankelma, and J.P. Baak, "Quantification by laser scan microscopy of intracellular doxorubicin distribution," Cytometry. **13**, 571-576 (1992).

7. J.E. Gervasoni, Jr., S.Z. Fields, S. Krishna, M.A. Baker, M. Rosado, K. Thuraisamy, A.A. Hindenburg, and R.N. Taub, "Subcellular distribution of daunorubicin in P-glycoprotein-positive and -negative drug-resistant cell lines using laser-assisted confocal microscopy," Cancer Res. **51**, 4955-4963 (1991).

8. H.M. Coley, W.B. Amos, P.R. Twentyman, and P. Workman, "Examination by laser scanning confocal fluorescence imaging microscopy of the subcellular localisation of anthracyclines in parent and multidrug resistant cell lines," British J. Cancer. **67**, 1316-1323 (1993).

9. J. Itoh, R.Y. Osamura, and K. Watanabe, "Subcellular visualization of light microscopic specimens by laser scanning microscopy and computer analysis: a new application of image analysis," J. Histochem. & Cytochem. **40**, 955-967 (1992).

10. K.W. Woodburn, N.J. Vardaxis, J.S. Hill, A.H. Kaye, and D.R. Phillips, "Subcellular localization of porphyrins using confocal laser scanning microscopy," Photochem. & Photobio. **54**, 725-732 (1991).

11. J.J. Andrew and T.M. Hancewicz, "Rapid analysis of Raman image data using two-way multivariate curve resolution," Appl. Spectrosc. **52**, 797-807 (1998).

12. N.J. Bauer, M. Motamedi, J.P. Wicksted, W.F. March, C.A. Webers, and F. Hendrikse, "Non-invasive assessment of ocular pharmacokinetics using Confocal Raman Spectroscopy," J. of Ocular Pharmaco. & Therapeutics. **15**, 123-134 (1999).

13. R. Manoharan, W. Yang, and M.S. Feld, "Histochemical analysis of biological tissues using Raman spectroscopy," Spectrochimica Acta Part A-Molecular Spectrosc. **52A**, 215-249 (1996).

14. K. Chinked, "Optical Diagnostics Image Tissues and Tumors," *in Laser Focus World*, 1996.

15. S.R. Goldstein, L.H. Kidder, T.M. Herne, I.W. Levin, and E.N. Lewis, "The design and implementation of a high-fidelity Raman imaging microscope," J. Microscopy. **184**, 35-45 (1996).

16. A. Feofanov, S. Sharonov, P. Valisa, E. Da Silva, I. Nabiev, and M. Manfait, "A new confocal stigmatic spectrometer for micro-Raman and microfluorescence spectral imaging analysis: Design and applications," Rev. Sci. Instrum. **66**, 3146-3158 (1995).

17. C.J.H. Brenan, I.W. Hunter, and M.J. Korenberg, "Volumetric Raman spectral imaging with a confocal Raman microscope: Image modalities and applications," Proc. SPIE. **2655**, 130-139 (1996).

18. M.D. Schaeberle, H.R. Morris, J.F. Turner II, and P.J. Treado, "Raman Chemical Imaging Spectroscopy," Anal. Chem. News & Features. March, 175A-181A (1999).

19. T.L. Freeman, S.E. Cope, M.R. Stringer, J.E. Cruse-Sawyer, S.B. Brown, D.N. Batchelder, and K. Birbeck, "Investigation of the subcellular localization of Zinc Phthalocyanines by Raman Mapping," Appl. Spectrosc. **52**, 1257-1263 (1998).

20. C.A. Drumm and M.D. Morris, "Microscopic Raman line-imaging with principal component analysis," Appl. Spectros. **49**, 1331-1337 (1995).

21. S.L. Zhang, J.A. Pezzuti, M.D. Morris, A. Appadwedula, C.M. Hsiung, M.A. Leugers, and D. Bank, "Hyperspectral Raman Line Imaging of Syndiotactic Polystyrene Crystallinity," Appl. Spectrosc. **52**, 1145-1147 (1998).

22. K.A. Christensen and M.D. Morris, "Hyperspectral Raman microscopic imaging using Powell lens line illumination," Appl. Spectrosc. **52**, 1145-1147 (1998).

23. G.J. Puppels and J. Greve, "Whole Cell Studies and Tissue Characterization By Raman Spectroscopy," in *Biomedical Applications of Spectroscopy*, C. Hester, Editor, John Wiley & Sons, Chichester. 1-47 (1996).

24. M.D. Schaeberle, V.F. Kalasinsky, J.L. Luke, E.N. Lewis, I.W. Levin, and P.J. Treado, "Raman chemical imaging: histopathology of inclusions in human breast tissue," Anal. Chem. **68**, 1829-1833 (1996).

25. H.R. Morris, C.C. Hoyt, P. Miller, and P.J. Treado, "Liquid crystal tunable filter Raman chemical imaging," Appl. Spectrosc. **50**, 805-811 (1996).

26. H.R. Morris, C.C. Hoyt, and P.J. Treado, "Imaging spectrometers for fluorescence and Raman microscopy: acousto-optic and liquid crystal tunable filters," Appl. Spectrosc. **48**, 857-866 (1994).

27. N.J. Kline and P.J. Treado, "Raman chemical imaging of breast tissue," J. Raman Spectrosc. **28**, 119-124 (1997).

28. C. Otto, C.J. de Grauw, J.J. Duindam, N.M. Sijtsema, and J. Greve, "Applications of micro-Raman imaging in biomedical research," J. Raman Spectrosc. **28**, 143-150 (1997).

29. N.M. Sijtsema, S.D. Wouters, C.J. De Grauw, C. Otto, and J. Greve, "Confocal direct imaging Raman microscope: design and applications in biology," Appl. Spectrosc. **52**, 348-355 (1998).

30. S.Y. Arzhantsev, A.Y. Chikishev, N.I. Koroteev, J. Greve, C. Otto, and N.M. Sijtsema, "Localization study of Co-phthalocyanines in cells by Raman micro(spectro)scopy," J. Raman Spectrosc. **30**, 205-208 (1999).

31. H. Parekh and H. Simpkins, "The transport and binding of taxol," General Pharmaco. **29**, 167-172 (1997).

32. B.Z. Leal, M.L. Meltz, N. Mohan, J. Kuhn, T.J. Prihoda, and T.S. Herman, "Interaction of hyperthermia with Taxol in human MCF-7 breast adenocarcinoma cells," International J. Hyperthermia. **15**, 225-236 (1999).

33. A.M. Yvon, P. Wadsworth, and M.A. Jordan, "Taxol suppresses dynamics of individual microtubules in living human tumor cells," Molecular Biol. of the Cell. **10**, 947-959 (1999).

34. K. Torres and S.B. Horwitz, "Mechanisms of Taxol-induced cell death are concentration dependent," Cancer Res. **58**, 3620-3626 (1998).

35. D.A. Agard, "Optical sectioning microscopy: cellular architecture in three dimensions," Ann. Rev. Biophy. & Bioeng. **13**, 191-219 (1984).

36. K.R. Castleman, *Digital Image Processing* (Prentice-Hall, Englewood Cliffs, New Jersey, 1995).

37. J. Ling, A. Bovik, "Smoothing Low SNR Molecular Images Via Anisotropic Median-Diffusion," IEEE Trans. Medical Imaging. **21**, (2002).

38. M.J. Black, G. Sapiro, D.H. Marimont, and D. Heeger, "Robust anisotropic diffusion," IEEE Trans. Image Proc. **7**, 421-432 (1998).

39. J. Ling, "The Development of Raman Imaging Microscopy To Visualize Drug Actions in Living Cells," Ph.D. Dissertation (The University of Texas at Austin, Austin, 2001), 150.

40. W.H. Richardson, "Bayesian-Based Iterative Method of Image Restoration," J. Opt. Soc. Am. **62**, 55-59 (1972).

41. Y.H. Lucy, "An Iterative Technique for the Rectification of Observed Distributions," Astronomy J. **79**, 745-765 (1974).

42. T.J. Holmes and Y.H. Liu, "Richardson-Lucy/maximum likelihood image restoration algorithm for fluorescence microscopy: further testing," Appl. Opt. **28**, 4930-4938 (1989).

43. G.M.P. van Kempen and L.J. van Vliet, "Background estimation in nonlinear image restoration," J. Opt. Soc. Am.- Opt. Image Sci. and Vision. **17**, 425-433 (2000).

44. B. Alberts, D. Bray, A. Johnson, J. Lewis, M. Raff, K. Robert, and P. Walter, "Microtubules," in *Essential Cell Biology - An Introduction to the Molecular Biology of the Cell*, Garland Publishing, New York. 518-529 (1998).

45. E.E. Morrison, J.M. Askham, P. Clissold, A.F. Markham, and D.M. Meredith, "The cellular distribution of the adenomatous polyposis coli tumour suppressor protein in neuroblastoma cells is regulated by microtubule dynamics," Neurosci. **81**, 553-563 (1997).

46. J.J. Lemasters, G.J. Gores, A.L. Nieminen, T.L. Dawson, B.E. Wray, and B. Herman, "Multiparameter digitized video microscopy of toxic and hypoxic injury in single cells," Enviro. Health Perspectives. **84**, 83-94 (1990).

47. W. Malorni, C. Fiorentini, S. Paradisi, M. Giuliano, P. Mastrantonio, and G. Donelli, "Surface blebbing and cytoskeletal changes induced in vitro by toxin B from

Clostridium difficile: an immunochemical and ultrastructural study," Exp. & Molecular Pathology. **52**, 340-356 (1990).

48. W. Malorni, F. Iosi, F. Mirabelli, and G. Bellomo, "Cytoskeleton as a target in menadione-induced oxidative stress in cultured mammalian cells: alterations underlying surface bleb formation," Chemico-Biological Interactions. **80**, 217-236 (1991).

49. M.S. Jurkowitz-Alexander, R.A. Altschuld, C.M. Hohl, J.D. Johnson, J.S. McDonald, T.D. Simmons, and L.A. Horrocks, "Cell swelling, blebbing, and death are dependent on ATP depletion and independent of calcium during chemical hypoxia in a glial cell line (ROC-1)," J. Neurochem. **59**, 344-352 (1992).

50. G. Zahrebelski, A.L. Nieminen, K. al-Ghoul, T. Qian, B. Herman, and J.J. Lemasters, "Progression of subcellular changes during chemical hypoxia to cultured rat hepatocytes: a laser scanning confocal microscopic study," Hepatology. **21**, 1361-1372 (1995).

51. S.M. Laster and J.M. Mackenzie, Jr., "Bleb formation and F-actin distribution during mitosis and tumor necrosis factor-induced apoptosis," Microscopy Res. & Tech. **34**, 272-280 (1996).

52. P.T. Jain and B.F. Trump, "Human breast cancer cell growth inhibition and deregulation of [Ca2+]i by estradiol," Anti-Cancer Drugs. **8**, 283-287 (1997).

53. T. Jones, "Present and future capabilities of molecular imaging techniques to understand brain function," J. Psychopharmaco. **13**, 324-329 (1999).

54. G.D. Sockalingum, A. Beljebbar, H. Morjani, J.F. Angiboust, and M. Manfait, "Characterization of island films as surface-enhanced Raman spectroscopy substrates for detecting low antitumor drug concentrations at single cell level," Biospectrosc. **4**, S71-78 (1998).

55. I.R. Nabiev, V.A. Savchenko, and E.S. Efremov, "Surface-enhanced Raman spectra of aromatic amino acids and proteins adsorbed by silver hydrosols," J. Raman Spectrosc. **14**, 375-379 (1983).

56. I.R. Nabiev, K.V. Sokolov, and O.N. Voloshin, "Surface-enhanced Raman spectroscopy of biomolecules III - Determination of the local destabilization regions in the double helix," J. Raman Spectrosc. **21**, 333-336 (1990).

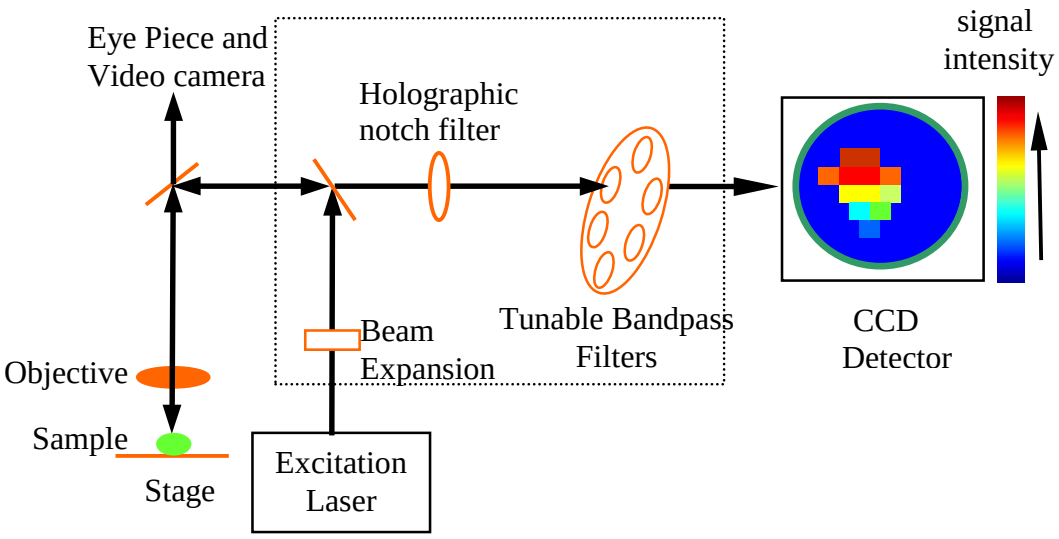

Fig. 1. Schematic diagram of a CCD-based direct Raman imaging system. This system is able to record the two-dimensional distribution of a specific type of molecule in a sample. The pseudo-color is used in the figure to indicate the signal intensity. The red area has higher intensity, indicating the molecule has higher concentration there. The dark blue area has low intensity, indicating there is less such molecule located there.

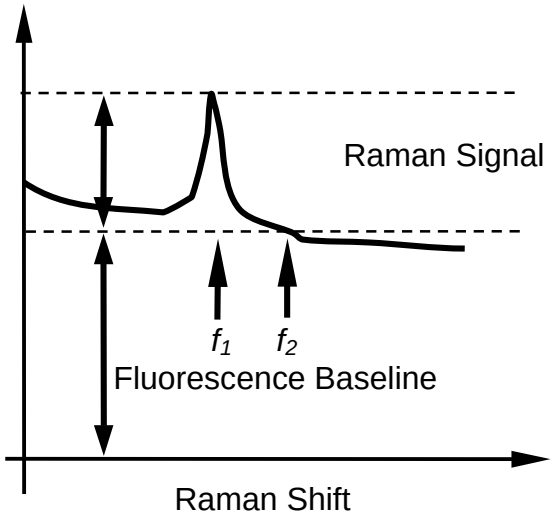

Fig. 2. Raman signals ride on a broad band fluorescence baseline for a Raman spectrum.

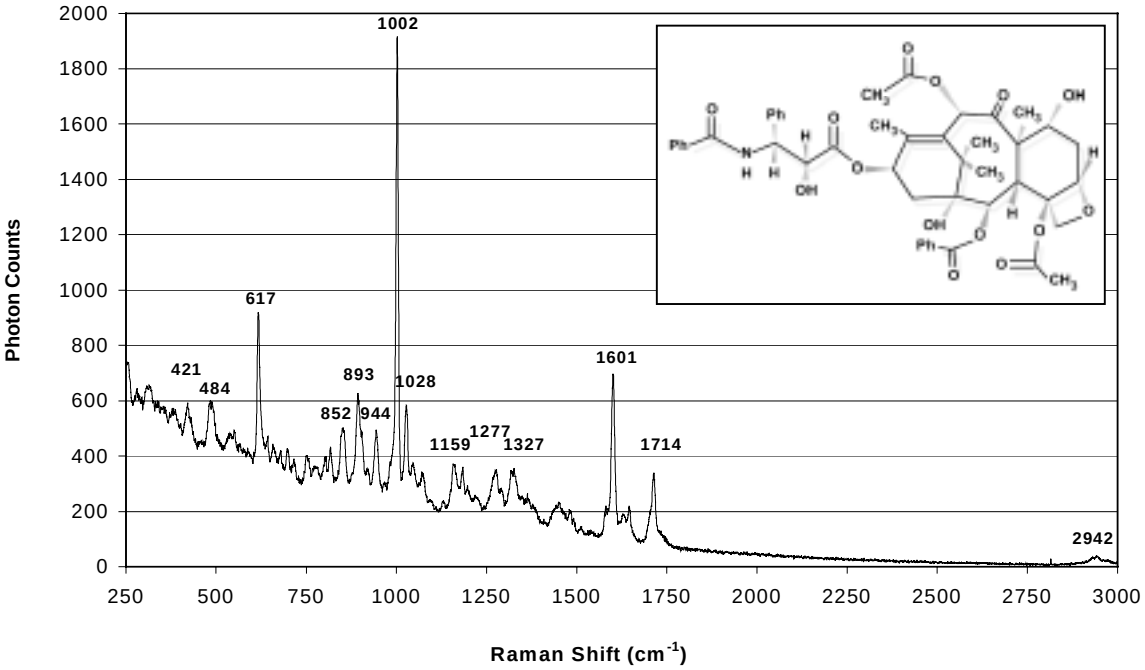

Fig. 3. Raman spectrum of paclitaxel (neat powder). The spectrum was taken with the 20X lens. The exposure time was 30 seconds. The insert is the chemical structure of paclitaxel.

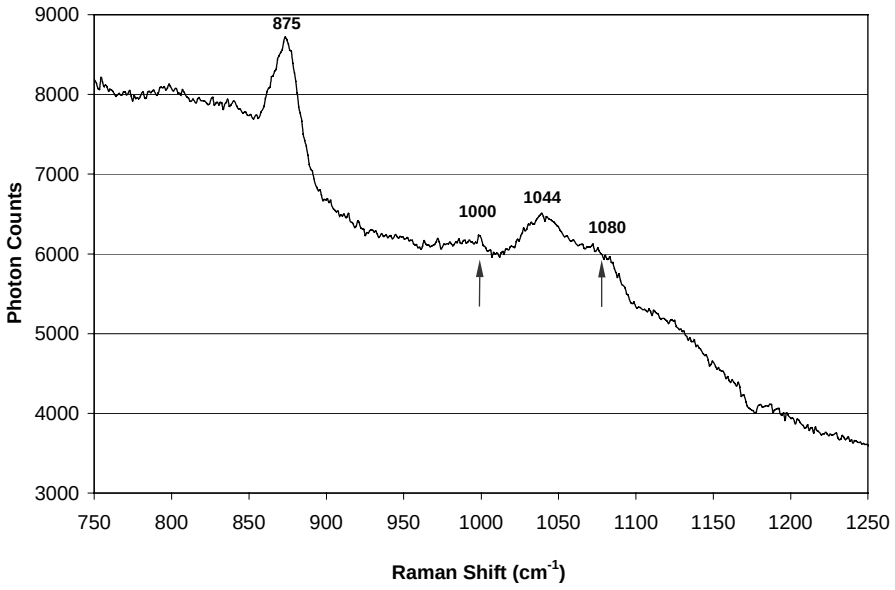

Fig. 4. Raman spectrum (between 750-1250 cm^{-1}) of 0.3 mg/ml (or 350 μM) paclitaxel solution, taken with the 60X W/IR lens and the exposure time of 300 seconds.

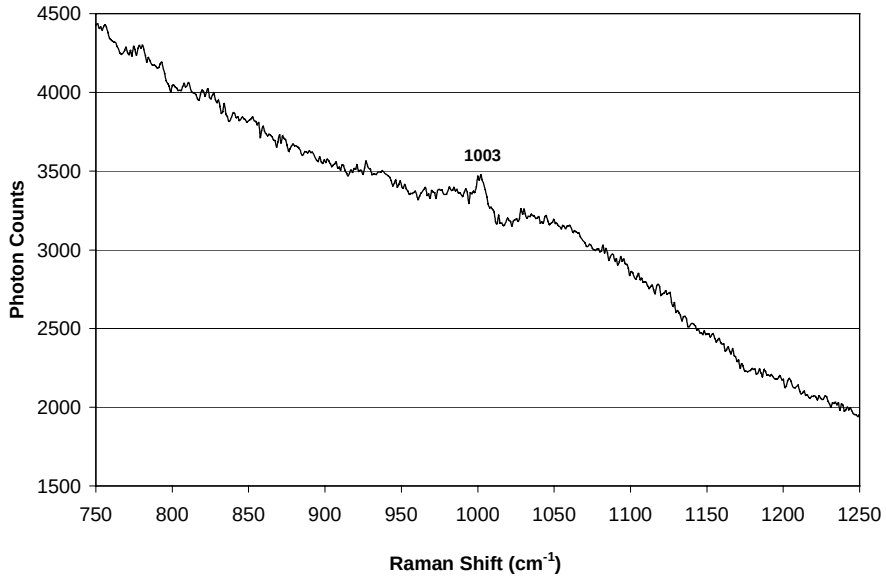

Fig. 5. Raman spectrum (750-1250 cm^{-1}) of cytoplasm from a MDA-435 tumor cell, taken with the 60X W/IR lens and the exposure time of 300 seconds. Raman spectrum of cell nucleus shows similar pattern.

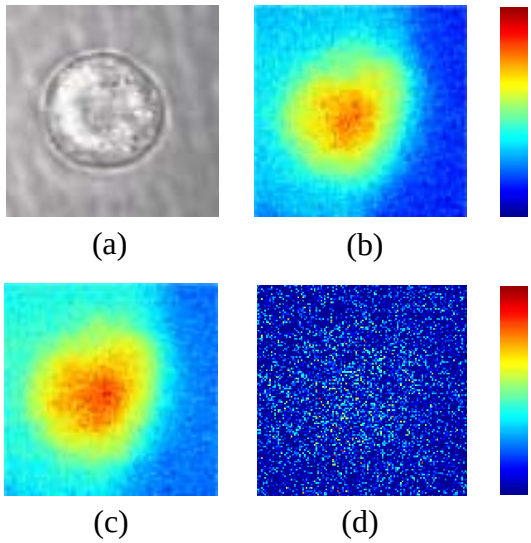

Fig. 6. An example of the image record. (a) The white light image of a MDA-435 breast cancer cell. (b) The Raman image of the cell taken at 1000 cm^{-1} Raman band using the 60x W/IR lens. The exposure time was 300 seconds. (c) The Raman image of the cell taken at 1080 cm^{-1} Raman band using the 60x W/IR lens. The exposure time was 300 seconds. (d) The difference of (b) and (c) before processing. The color bar indicates the relative Raman signal intensity increasing from bottom to top.

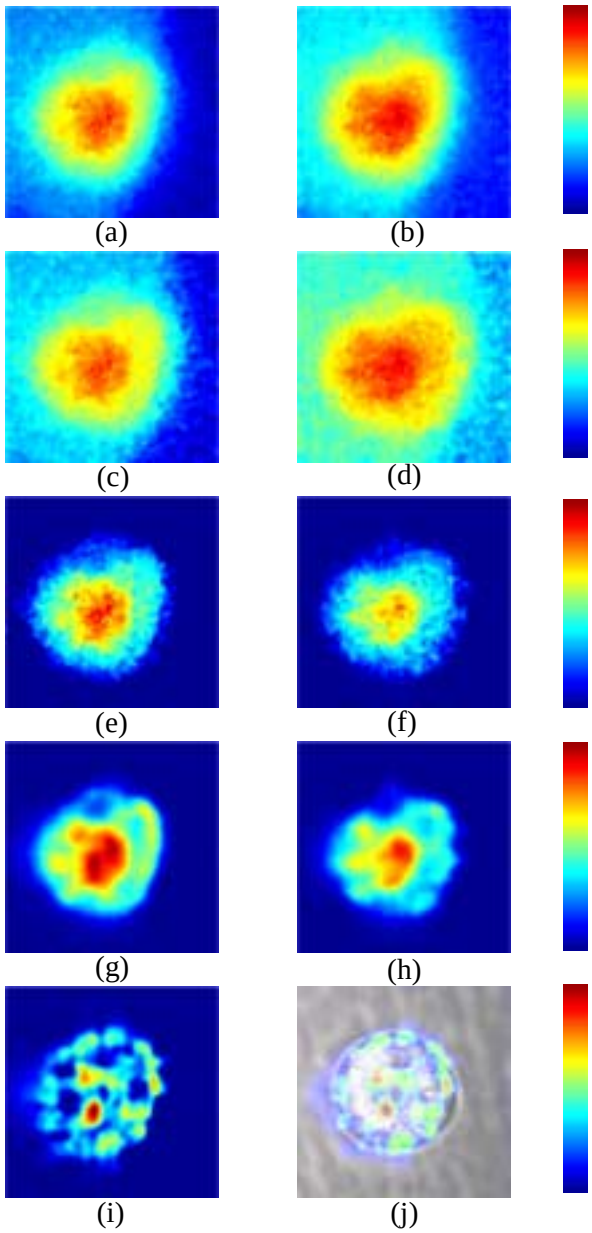

Fig. 7. Post-processing of Raman images in Figure 6(b) and 6(c) are illustrated in left and right columns, respectively. (a) and (b): Smoothed images; (c) and (d): Non-uniform illumination corrected images; (e) and (f): Background subtracted images; (g) and (h): Three-dimensional blur restored images; (i): Fluorescent signal eliminated image; (j) Overlay of the image of (i) on the image in Figure 6(a). The color bars indicate the relative Raman signal intensity increasing from bottom to top.

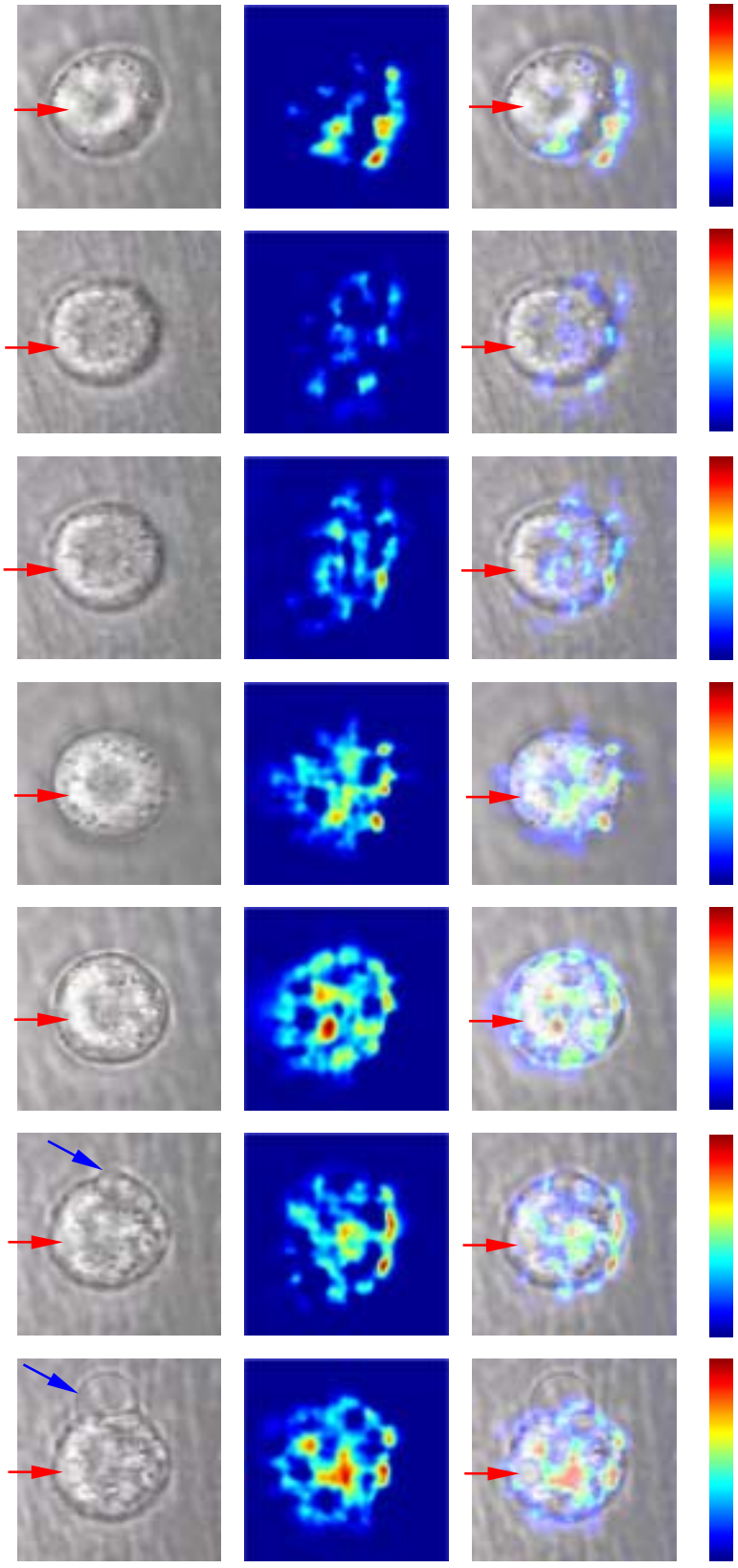

Fig. 8. Images before, during, and after an MDA-435 breast cancer cell was exposed to the paclitaxel agent. The first row illustrates the images before drug treatment. The second and third rows illustrate the images 10 minutes and 45 minutes during the drug treatment. The fourth row to seventh row illustrate the images 10 minutes, 1.75 hours, 4 hours, and 4.5 hours after the drug treatment. The left column is the white light images of the cell that show the cell structure. The center column is the Raman images of the cell that show the intensity distribution in the 1000 cm^{-1} Raman band. The right column is the overlay of images in the left and center columns. The red arrows point to the cell nucleus region. The blue arrows point to the cell blebbing region. The color bar indicates the relative Raman signal intensity increasing from bottom to top.

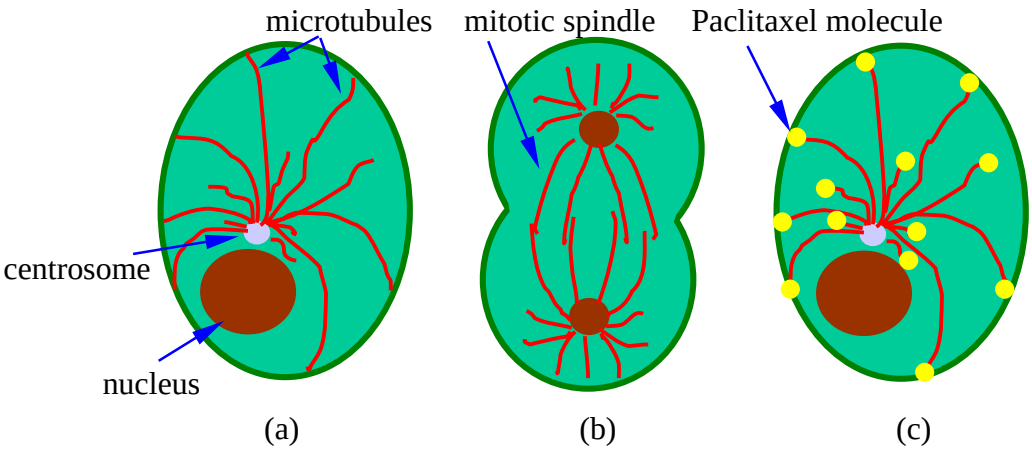

Fig. 9. Distribution and functions of the cell microtubules. (a) Microtubules grow out from the centrosome and extend to cell membrane. (b) In the dividing cell, microtubules form a mitotic spindle to help nucleus splitting. (c) Paclitaxel binds to the growth end of the microtubules.

Figure Captions

Fig. 1. Schematic diagram of a CCD-based direct Raman imaging system. This system is able to record the two-dimensional distribution of a specific type of molecule in a sample. The pseudo-color is used in the figure to indicate the signal intensity. The red area has higher intensity, indicating the molecule has higher concentration there. The dark blue area has low intensity, indicating there is less such molecule located there.

Fig. 2. Raman signals ride on a broad band fluorescence baseline for a Raman spectrum.

Fig. 3. Raman spectrum of paclitaxel (neat powder). The spectrum was taken with the 20X lens. The exposure time was 30 seconds. The insert is the chemical structure of paclitaxel.

Fig. 4. Raman spectrum (between 750-1250 cm^{-1}) of 0.3 mg/ml (or 350 μM) paclitaxel solution, taken with the 60X W/IR lens and the exposure time of 300 seconds.

Fig. 5. Raman spectrum (750-1250 cm^{-1}) of cytoplasm from a MDA-435 tumor cell, taken with the 60X W/IR lens and the exposure time of 300 seconds. Raman spectrum of cell nucleus shows similar pattern.

Fig. 6. An example of the image record. (a) The white light image of a MDA-435 breast cancer cell. (b) The Raman image of the cell taken at 1000 cm^{-1} Raman band using the 60x W/IR lens. The exposure time was 300 seconds. (c) The Raman image of the cell taken at 1080 cm^{-1} Raman band using the 60x W/IR lens. The exposure time was 300 seconds. (d) The difference of (b) and (c) before processing. The color bar indicates the relative Raman signal intensity increasing from bottom to top.

Fig. 7. Post-processing of Raman images in Figure 6(b) and 6(c) are illustrated in left and right columns, respectively. (a) and (b): Smoothed images; (c) and (d): Non-uniform illumination corrected images; (e) and (f): Background subtracted images; (g) and (h): Three-dimensional blur restored images; (i): Fluorescent signal eliminated image; (j) Overlay of the image of (i) on the image in Figure 6(a). The color bars indicate the relative Raman signal intensity increasing from bottom to top.

Fig. 8. Images before, during, and after an MDA-435 breast cancer cell was exposed to the paclitaxel agent. The first row illustrates the images before drug treatment. The second and third rows illustrate the images 10 minutes and 45 minutes during the drug treatment. The fourth row to seventh row illustrate the images 10 minutes, 1.75 hours, 4 hours, and 4.5 hours after the drug treatment. The left column is the white light images of the cell that show the cell structure. The center column is the Raman images of the cell that show the intensity distribution in the 1000 cm^{-1} Raman band. The right column is the overlay of images in the left and center columns. The red arrows point to the cell nucleus

region. The blue arrows point to the cell blebbing region. The color bar indicates the relative Raman signal intensity increasing from bottom to top.

Fig. 9. Distribution and functions of the cell microtubules. (a) Microtubules grow out from the centrosome and extend to cell membrane. (b) In the dividing cell, microtubules form a mitotic spindle to help nucleus splitting. (c) Paclitaxel binds to the growth end of the microtubules.